Quantifying nanoscale forces using machine learning in dynamic atomic force microscopy

Abhilash Chandrashekar,[1,*] Pierpaolo Belardinelli,[2] Miguel A. Bessa,[3] Urs Staufer,[1] and Farbod Alijani[1,†]

[1]*Precision and Microsystems Engineering, TU Delft, Delft, The Netherlands*
[2]*DICEA, Polytechnic University of Marche, Ancona, Italy*
[3]*Material Science and Engineering, TU Delft, Delft, The Netherlands*

(Dated: January 4, 2022)

S1: ADDITIONAL DATA: ALGORITHM TRAINING

In this section we report additional results from training the data-driven algorithm. Training data is derived from various well-established AFM models with different interaction physics. In particular, we utilized the following models for the training and validation of the algorithm:

A. Derjaguin-Muller-Toporov (DMT) model[1];

B. Lennard-Jones model.

C. DMT model with viscoelastic damping.

D. DMT model with exponential damping.

E. JKR model.

Models and results of the training are detailed in the next subsections.

A. DMT model

The equation of motion governing the AFM dynamics undergoing DMT interaction is given by Eq. 1. Here, the cantilever tip deflection towards the sample is denoted by x and the instantaneous tip-sample distance and the indentation depth are indicated by z and δ, respectively. It should be noted that both z and δ are functions of x. The damping and stiffness coefficients are indicated by D and K, the amplitude of the dither piezoelectric actuator is denoted by B. The dotted quantities represent derivatives with respect to the re-scaled time τ ($\tau = \omega_0 t$), where ω_0 is the natural frequency of the cantilever. In the DMT model, the tip-sample force F_{ts} consists of: i) long range Van der Waals attractive force with coefficient C_1 governed by a second order inverse power law; ii) repulsive component described by the Hertz contact force with effective stiffness governed by the coefficient C_2; iii) adhesion force given by $F_a = 4\pi R\gamma$ with R and γ representing the AFM tip radius and surface interaction energy, respectively. The adhesion force F_a can be reformulated as an attractive force such that it depends on the intermolecular distance a_0 and its strength is governed by the coefficient C_3. The coefficients utilized for the simulations are that of reference article. [1, 2]. The results of this model are discussed in the main manuscript.

$$
\begin{aligned}
&\ddot{x} + D\dot{x} + Kx = F_{ts}(z) + B\cos(\Omega\tau) \\
&F_{ts}(z) = \begin{cases} C_1/z^2, & \text{for} \quad z > a_0 \\ C_2(\delta)^{3/2} - F_a, & \text{for} \quad z \leq \bar{a}_0. \end{cases} \\
&F_a = 4\pi R\gamma = C_3/{a_0}^2.
\end{aligned}
\tag{1}
$$

---

* a.chandrashekar@tudelft.nl
† f.alijani@tudelft.nl

[1] Model employed to train the sparse identification algorithm in the main manuscript. Training outcome is shown in the main manuscript in Fig. 1 with description of the library functions in Tab. 1.

B. Lennard-Jones model

In the Lennard-Jones (LJ) force model the tip-sample interaction is described by the continuous and smooth functions of Eq. 2:

$$\begin{aligned} \ddot{x} + D\dot{x} + Kx &= F_{ts}(z) + B\cos(\Omega\tau) \\ F_{ts}(z) &= C_1/z^2 + C_2/z^8 . \end{aligned} \tag{2}$$

The tip-sample force F_{ts} consists of Van der Waals attractive force comprising a second and an eighth order inverse power law function of the instantaneous tip-sample separation z and proportional to the coefficients C_1 and C_2, respectively. Additional parameters in Eq. 2 related to the cantilever dynamics are those of Eq. 1 and described in Sec. A. The coefficients for the simulations are obtained from the reference article [3, 4].

Figures. S1.1 (a) & (b) highlight the transient and steady state dynamics as determined by the data-driven analysis. In addition to the state vectors, Figs. S1.1 (c) & (d) show the transient and steady state tip-sample force. In either of the cases the blue and orange colours indicate the original and identified responses. Furthermore, Fig. S1.2 shows the coefficients obtained from the data-driven algorithm in comparison with the values used in simulation; whereas table I provides an insight into the library functions used in the simulation. It must be noted that since the model is governed by a smooth and continuous tip-sample force with relatively simple functions, the LJ model shows the fastest convergence rate among all the tested models.

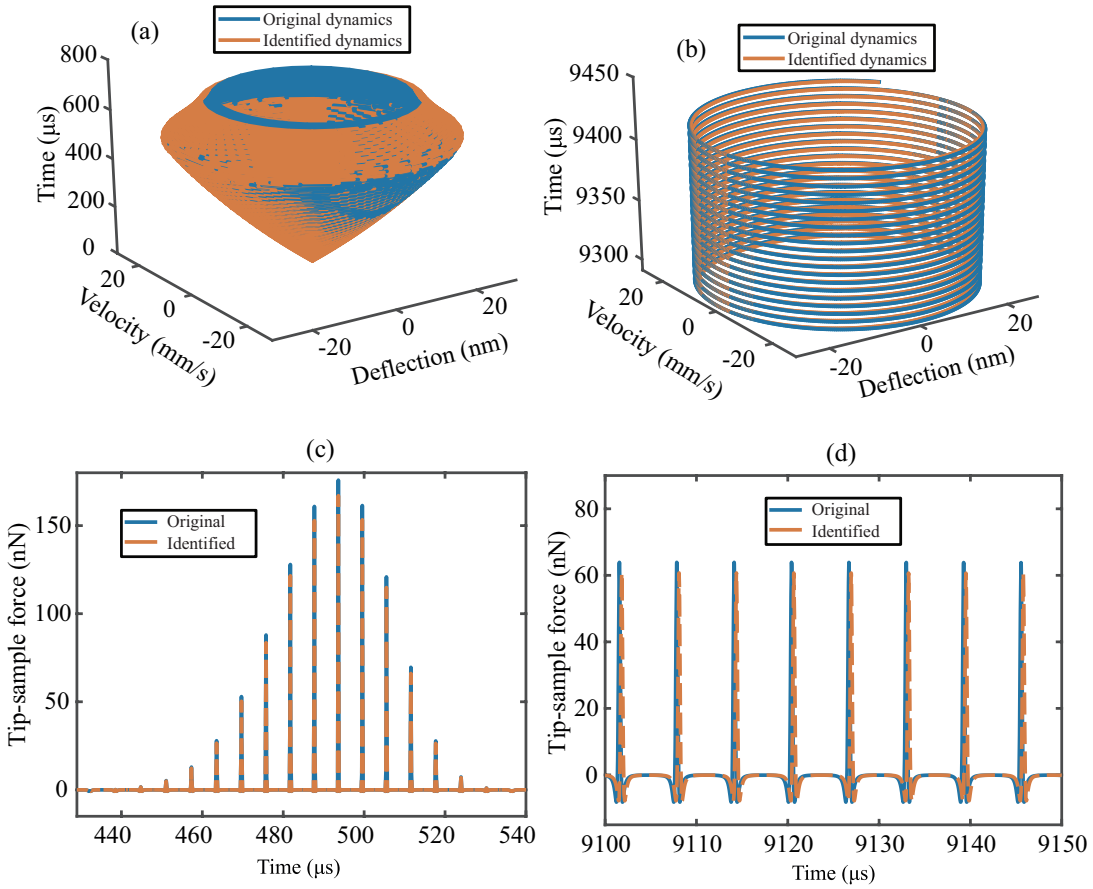

FIG. S1.1: Simulations of a cantilever interacting with a sample based on LJ force model. The LJ model parameters are tuned to induce transient and steady state dynamics in order to replicate the experiments. (a) Transient dynamics prediction: The blue curve indicates the simulated transient phase space trajectory and the orange curve is the prediction from the data-driven model. (b) Steady state dynamics prediction: The blue curve indicates the simulated steady state phase space trajectory and the orange curve shows prediction from the data-driven model. (c)-(d) Comparison of the tip sample force between the LJ simulation (blue) and the data-driven model (orange) for both the transient and steady state scenarios. The coefficients utilized for the simulations are that of Rutzel et al. [3, 4]

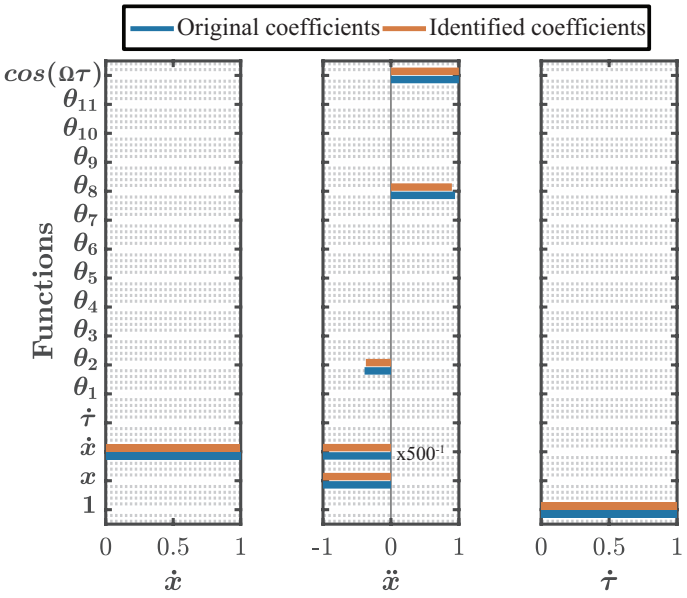

FIG. S1.2: Coefficient matrix showing the influence of each library function on the governing equations of LJ force model. The blue color indicates the original value of the coefficients and the orange color indicates the coefficients as determined by the data-driven model. The θ_i functions are detailed in Tab. I

TABLE I: Description of the nonlinear functions used in the coefficient matrix of Fig. S1.2.

Function ID	$\theta_1 to \theta_8$	θ_9	θ_{10}	θ_{11}
Function definition	z^{-n} , n=1 to 8	$z^{1.5}$	z^2	sin($\Omega\tau$)

C. DMT model with viscoelastic damping

The third stage of the training is performed employing a standard DMT model with an additional viscoelastic term in the interaction mechanism. Viscoelasticity plays an important role in the energy dissipation mechanisms when dealing with soft samples, e.g. polymers and biological specimens [5–7]. Identification of these dissipation mechanisms is crucial to understand the hysteresis observed in experiments. Equation. 3 describes the DMT model accounting for the viscoelastic behaviour. The basic mathematical model is that of Eq. 1, adding a viscoelastic contribution controlled by the coefficient C_4 that depends on the rate of indentation ($\dot{\delta}$). Similar to the LJ model, the amplitude of deflection is described with x, the instantaneous tip-sample distance by z and the indentation depth by δ. The coefficients utilized for the simulations are derived from the reference articles [1, 5, 6]. Contrary to the LJ model, the DMT model with viscoelastic terms contains both conservative and dissipative nature of interaction and represents a closer picture to what is encountered in an experimental scenario.

$$
\begin{aligned}
&\ddot{x} + D\dot{x} + Kx = F_{ts}(z,\dot{z}) + B\cos(\Omega\tau) \\
&F_{ts}(z,\dot{z}) = \begin{cases} C_1/z^2, & \text{for} \quad z > a_0 \\ C_2(\delta)^{3/2} - C_4\sqrt{\delta}\dot{\delta} - F_a, & \text{for} \quad z \le \bar{a}_0. \end{cases} \\
&F_a = 4\pi R\gamma = C_3/{a_0}^2
\end{aligned}
\tag{3}
$$

Figures. S1.3 (a) and (b) highlight the transient and steady state dynamics as determined by the data-driven analysis. In addition, Figs. S1.3 (c) and (d) show the simulated and reconstructed tip-sample force for the transient and steady state case. The coefficients extracted from the data-driven approach are compared with those of the simulations in Fig. S1.4. The difference in the identified coefficients leads to a phase drift of the identified trajectory and visible in Fig. S1.3(d). The description of the library functions used in the simulation is reported in table II. The algorithm identifies three additional functions with respect to those in Eq. 3: i) $\theta_2 = z^{-3}$, in combination with θ_1 is used by the algorithm for estimating long range attractive forces; ii) $\theta_{11} = \sin(\tau)$, function that is similar to the excitation function $cos(\tau)$ but with a 90 deg phase difference; iii) θ_{10}, a bridging function similar to the constant term described by F_a in Eq. 3. These additional functions help to accommodate the perturbation in the dynamics due to the presence of noise.

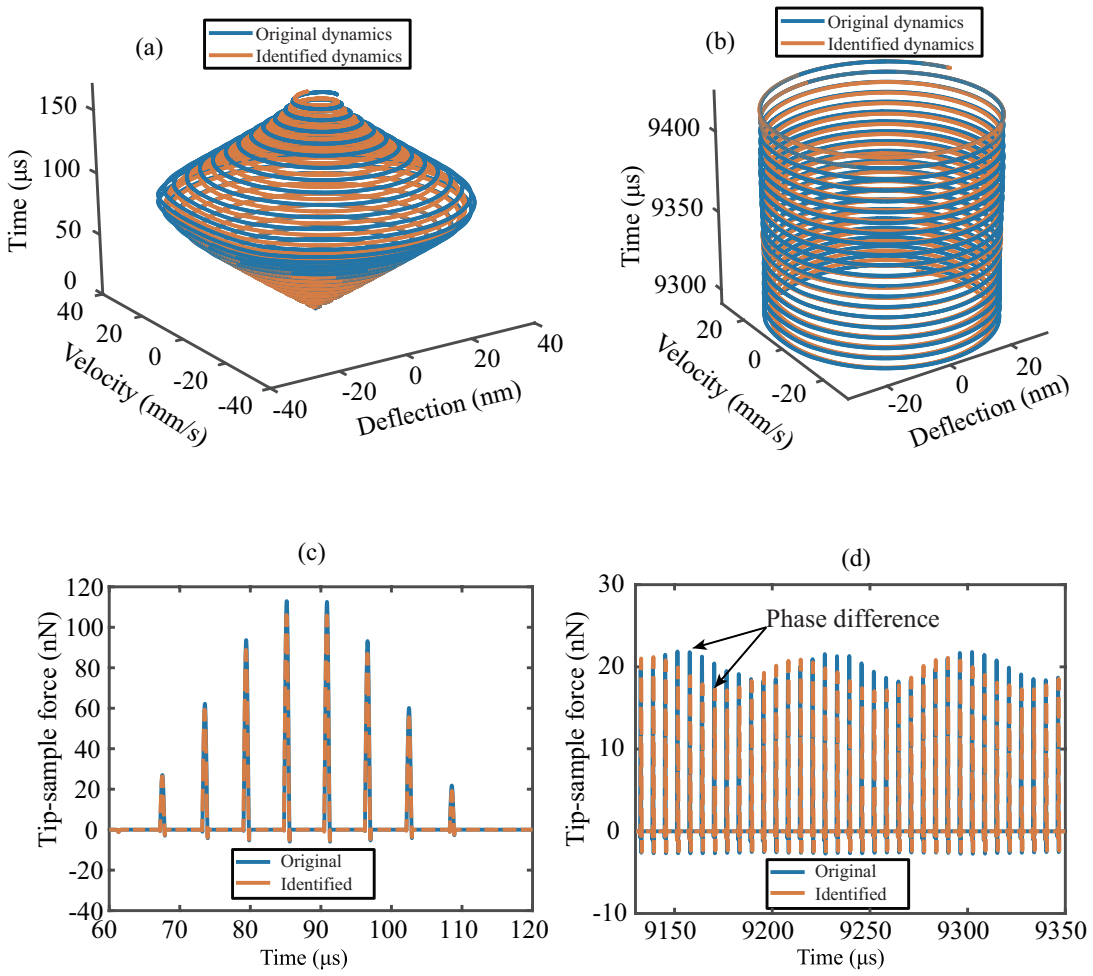

FIG. S1.3: Simulations of a cantilever interacting with a sample based on DMT force model with additional viscoelastic interaction. The model parameters are tuned to induce transient and steady state dynamics in order to replicate the experiments. (a) Transient dynamics prediction: The blue curve indicates the simulated transient phase space trajectory and the orange curve is the prediction from the data-driven model. (b) Steady state dynamics prediction: The blue curve indicates the simulated steady state phase space trajectory and the orange curve shows prediction from the data-driven model. (c)-(d) Comparison of the tip sample force between the simulation (blue) and the data-driven model (orange) for both the transient and steady state scenarios.

TABLE II: Description of the nonlinear functions used in the coefficient matrix of Fig. S1.4.

Function ID	θ_1	θ_2	θ_3	θ_4	θ_5	θ_6	θ_7	θ_8	θ_9	θ_{10}	θ_{11}
Function definition	z^{-2}	z^{-3}	$\delta^{0.5}\,\dot{\delta}$	$\delta\,\dot{\delta}^2$	$z^{0.5}\,\dot{z}$	$z\dot{z}^2$	δ^2	$\delta^{2.5}$	$\delta^{1.5}$	$z^{-2}\ \forall z \leq a_0$	$\sin(\Omega\tau)$

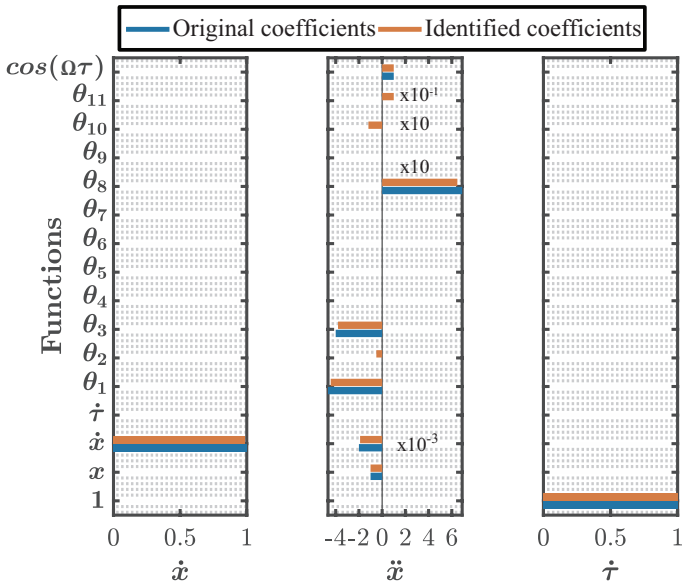

FIG. S1.4: Coefficient matrix showing the influence of each library function on the governing equations of DMT force model with additional viscoelastic interactions. The blue color indicates the original value of the coefficients and the orange color indicates the coefficients as determined by the data-driven model.

D. DMT with exponential damping

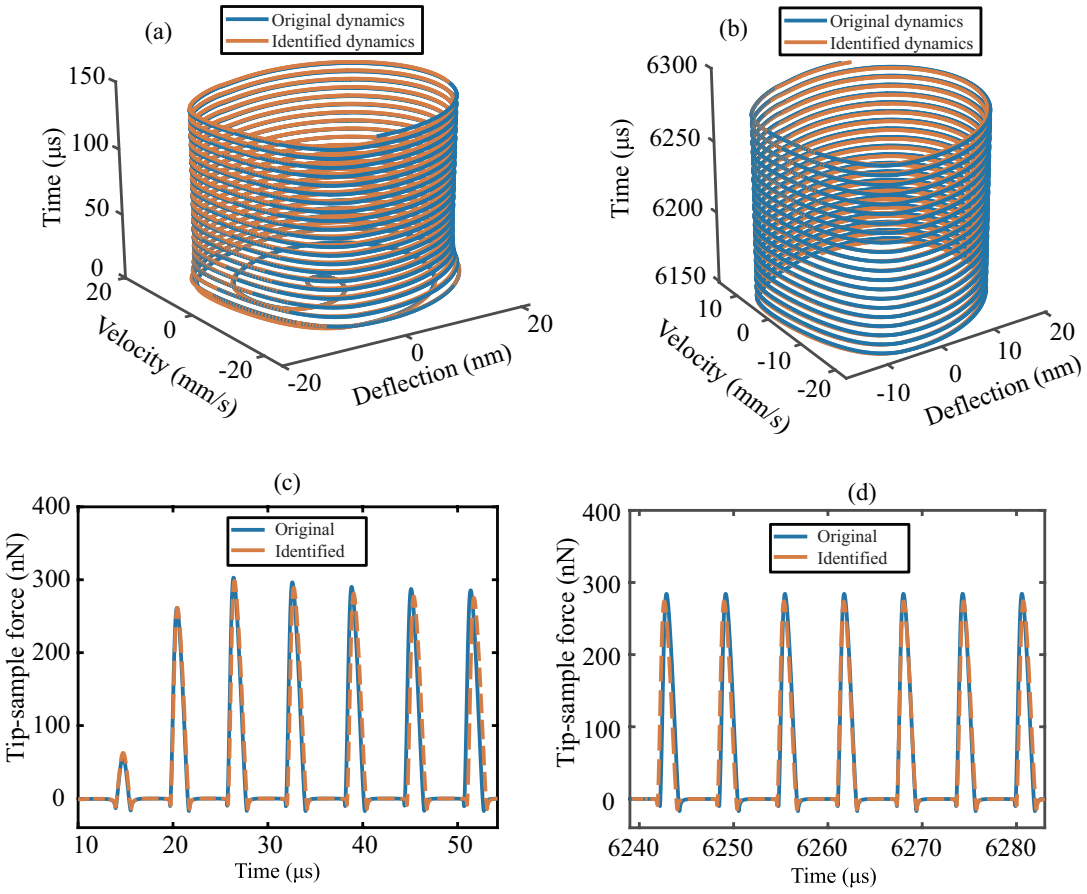

FIG. S1.5: Simulations of a cantilever interacting with a sample based on DMT force model with additional exponential damping term. The model parameters are tuned to induce transient and steady state dynamics in order to replicate the behaviour found in experiments. (a) Transient dynamics prediction: The blue curve indicates the simulated transient phase space trajectory and the orange curve is the prediction from the data-driven model. (b) Steady state dynamics prediction: The blue curve indicates the simulated steady state phase space trajectory and the orange curve shows prediction from the data-driven model. (c)-(d) Comparison of the tip sample force between the simulation (blue) and the data-driven model (orange) for both the transient and steady state scenarios.

This stage of the training sees the DMT model augmented with exponential damping term in the interaction mechanism (Eq. 4). The exponential damping term captures the capillary forces, adhesion and other surface forces with certain decay length [8]. In turn they contribute to the hysteresis in the interaction. The exponential damping term in Eq. 4 is governed by the coefficient C_4 and depends on the instantaneous tip-sample distance z and the instantaneous velocity $\dot{z}$, contributing to the non-dissipative nature of interaction. Furthermore, in a similar fashion to the aforementioned models, the amplitude of deflection is governed by x, the indentation depth by δ and the decay length of the exponential damping by z_β. The coefficients utilized for the simulations are derived from the reference articles [8].

$$
\begin{aligned}
&\ddot{x} + D\dot{x} + Kx = F_{ts}(z,\dot{z}) + B\cos(\Omega\tau) \\
&F_{ts}(z,\dot{z}) = \begin{cases} C_1/z^2 - C_4\, exp(z/z_\beta)\dot{z}, & \text{for} \quad z > a_0 \\ C_2(\delta)^{3/2} - F_a - C_4\, exp(z/z_\beta)\dot{z}, & \text{for} \quad z \leq \bar{a}_0. \end{cases} \\
&F_a = 4\pi R\gamma = C_3/{a_0}^2
\end{aligned}
\tag{4}
$$

Figures S1.5 (a) and (b) illustrate the transient and steady state dynamics as determined by the data-driven analysis. In addition to the state vectors, Figs. S1.5 (c) and (d) report the transient and steady state tip-sample force. The coefficients obtained from

the data-driven algorithm are listed in Fig. S1.6. The data-driven reconstruction with DMT model and exponential damping does not highlight the phase shift of Sec. C. The library functions used in the simulation is in Tab. III. Again we observe three additional functions in the identification. The functions θ_2 described by z^{-3} and θ_9 described by $z\dot{z}$ arise due to the presence of noise. Whereas, the function θ_{10} acts as a bridging function similar to the constant term described by F_a in Eq. 4.

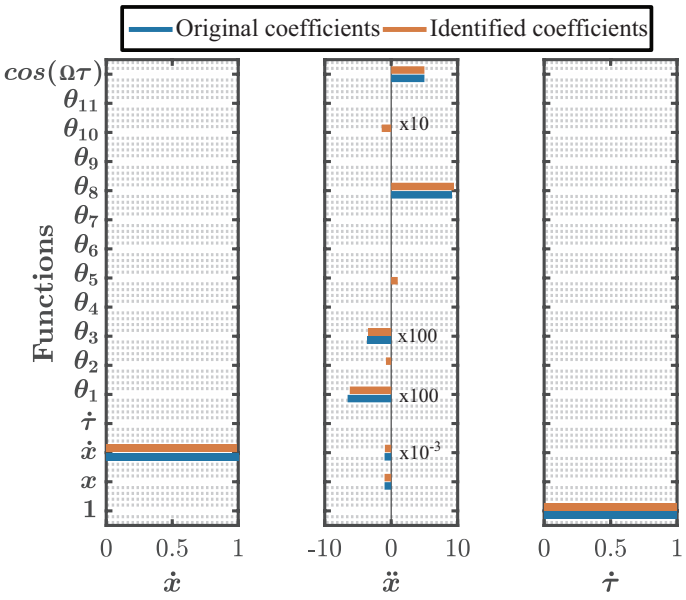

FIG. S1.6: Coefficient matrix showing the influence of each library function on the governing equations of DMT force model with additional exponential damping. The blue color indicates the original value of the coefficients and the orange color indicates the coefficients as determined by the data-driven model. The θ_i functions are detailed in Tab. III.

TABLE III: Description of the nonlinear functions used in the coefficient matrix of Fig. S1.6.

Function ID	θ_1	θ_2	θ_3	θ_4	θ_5	θ_6	θ_7	θ_8	θ_9	θ_{10}	θ_{11}
Function definition	z^{-2}	z^{-3}	$exp(z/z_\beta)\dot{z}$	$exp(z/z_\beta)^2\dot{z}^2$	$z\dot{z}$	$z\dot{z}^2$	δ^2	$\delta^{2.5}$	$\delta^{1.5}$	$z^{-2}\ \forall z \leq a_0$	$\sin(\Omega\tau)$

E. JKR model

The last stage of the training is performed with a Johnson, Kendall and Roberts (JKR) force model. The JKR model is particularly suited for AFM cantilever with large tip radius and large adhesion forces, which are regularly encountered in biological and soft polymers [9]. The equation describing the tip-sample interaction is shown in Eq. 5. Here, the tip-sample force F_{ts} consists of long range Van der Waals attractive force with coefficient C_1 governed by a second order inverse power law. The contact mechanics is described by the Hertz contact force with effective stiffness governed by the coefficient C_2, and the adhesion force given by F_a similar to the DMT model used in the main manuscript. However, in case of JKR model the adhesion force given by $F_a = 3\pi R\gamma$ is in general larger in amplitude due to larger tip radius and surface energy and thus leads to larger dissipation and hysteresis during the pull off event. Once gain, here R and γ are the AFM tip radius and surface interaction energy respectively. Similar to Eq. 3, the adhesion force F_a translates into an attractive force that depends on the intermolecular distance a_0 and its strength governed by the coefficient C_4.

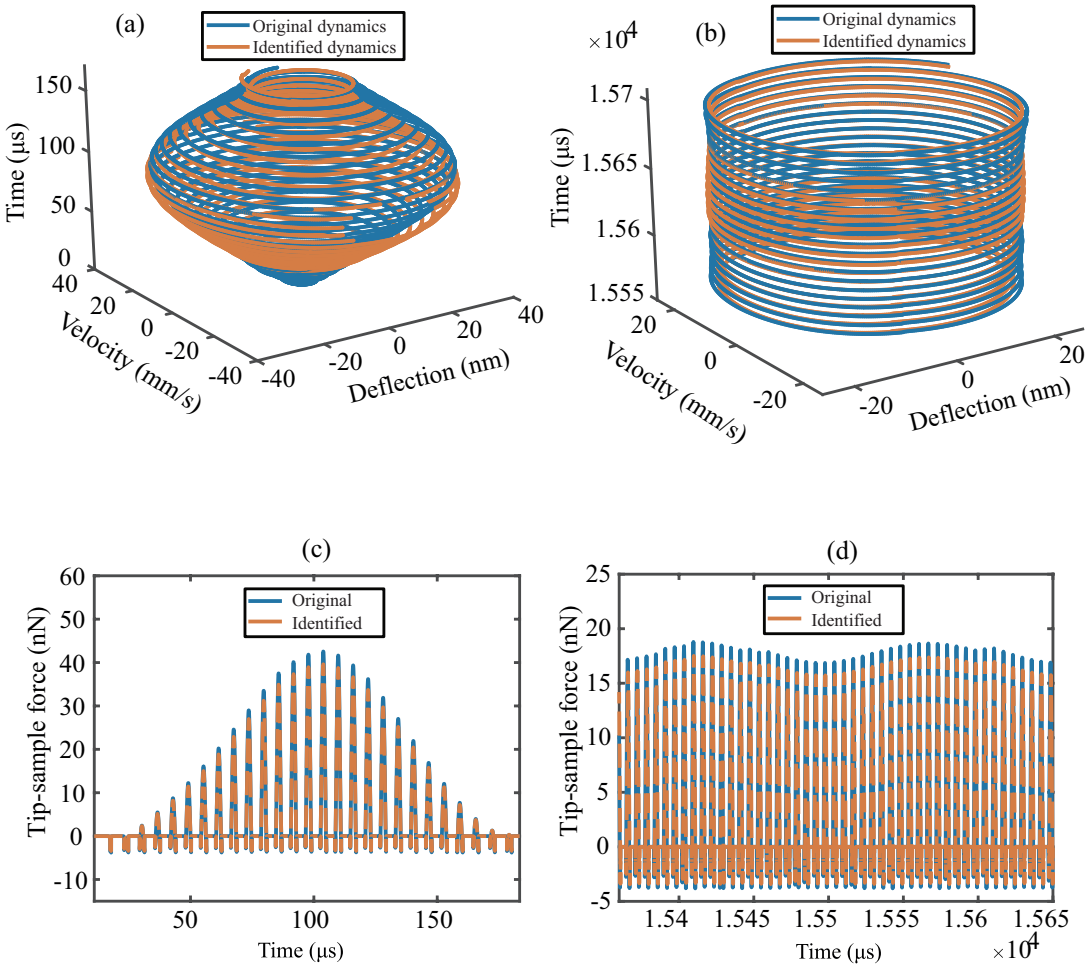

FIG. S1.7: Simulations of a cantilever interacting with a sample based on JKR force model used in the training stage of the data-driven model. The model parameters are tuned to induce transient and steady state dynamics in order to replicate the behaviour found in experiments. (a) Transient dynamics prediction: The blue curve indicates the simulated transient phase space trajectory and the orange curve is the prediction from the data-driven model. (b) Steady state dynamics prediction: The blue curve indicates the simulated steady state phase space trajectory and the orange curve shows prediction from the data-driven model. (c)-(d) Comparison of the tip sample force between the simulation (blue) and the data-driven model (orange) for both the transient and steady state scenarios. The coefficients utilized for the simulations are derived from the reference article [10].

$$\ddot{x} + D\dot{x} + Kx = F_{ts}(z,\dot{z}) + B\cos(\Omega\tau)$$
$$F_{ts}(z,\dot{z}) = \begin{cases} C_1/z^2, & \text{for} \quad z > a_0 \\ C_2(\delta)^{3/2} - F_a, & \text{for} \quad z \leq \bar{a}_0. \end{cases} \tag{5}$$
$$F_a = 3\pi R\gamma = C_3/{a_0}^2$$

The dynamics of the system described by a JKR interaction force resembles that of the DMT model in the main manuscript as observed in Figs. S1.7 (a) and (b). The data-driven algorithm is able to accurately capture the governing dynamics with a small phase difference which occurs once again due to the presence of noise. The Reconstruction of transient and steady state tip-sample force is reported in Figs. S1.7 (c) and (d). Here, in contrast to the DMT model, the presence of a larger adhesion force during the pull off of the cantilever results in larger hysteresis as observed in Figs. S1.7 (c) and (d). Furthermore, Fig. S1.8 shows the coefficients obtained from the data-driven algorithm in comparison with the values used for simulation. Due to similar nature of the functions required to described both the JKR and DMT models, we utilize the same library used for the DMT model in main manuscript (Tab. 1) to describe the JKR force interactions as well which highlights the interchangeability and universal nature of the technique.

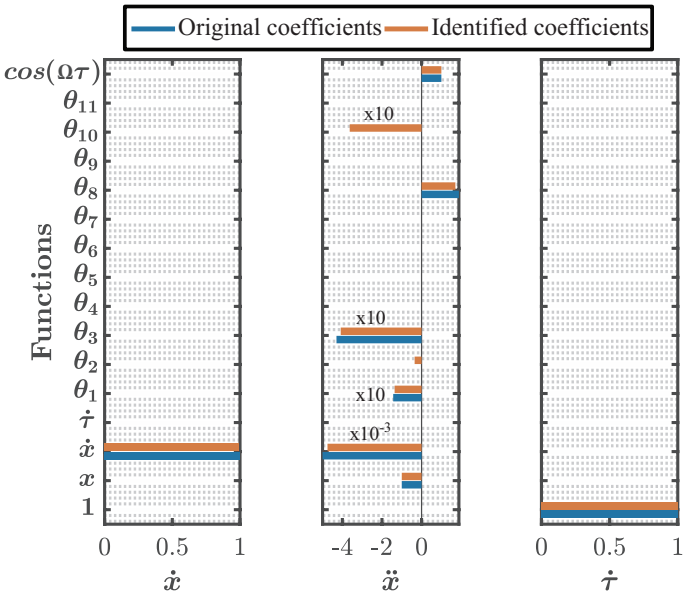

FIG. S1.8: Coefficient matrix showing the influence of each library function on the governing equations of JKR force model. The blue color indicates the original value of the coefficients and the orange color indicates the coefficients as determined by the data-driven model. The θ_i functions are detailed in Tab. IV.

TABLE IV: Description of the nonlinear functions used in the coefficient matrix of Fig. S1.8.

Function ID	θ_1	θ_2	θ_3	θ_4	θ_5	θ_6	θ_7	θ_8	θ_9	θ_{10}	θ_{11}
Function definition	z^{-2}	z^{-3}	$\delta^{0.5}\,\dot{\delta}$	$\delta\,\dot{\delta}^2$	$z^{0.5}\,\dot{z}$	$z\dot{z}^2$	δ^2	$\delta^{2.5}$	$\delta^{1.5}$	$z^{-2}\ \forall z \leq a_0$	$\sin(\Omega\tau)$

S2: ADDITIONAL EXPERIMENTAL RESULTS

F. Identification of tip-sample interaction in LDPE sample

Figure S2.9 reports the data-driven identification for a silicon cantilever interacting with a LDPE sample. The presentation of the results is similar to that of Fig. 3 of the main manuscript. We acquire a total of 50 periods of time oscillations obtained at a fixed distance of 63.1 nm from the sample. We performed data-driven analysis to identify the dynamics (Fig. S2.9(a)) and to capture the variation of the instantaneous tip-sample force period by period (Fig. S2.9(b)).

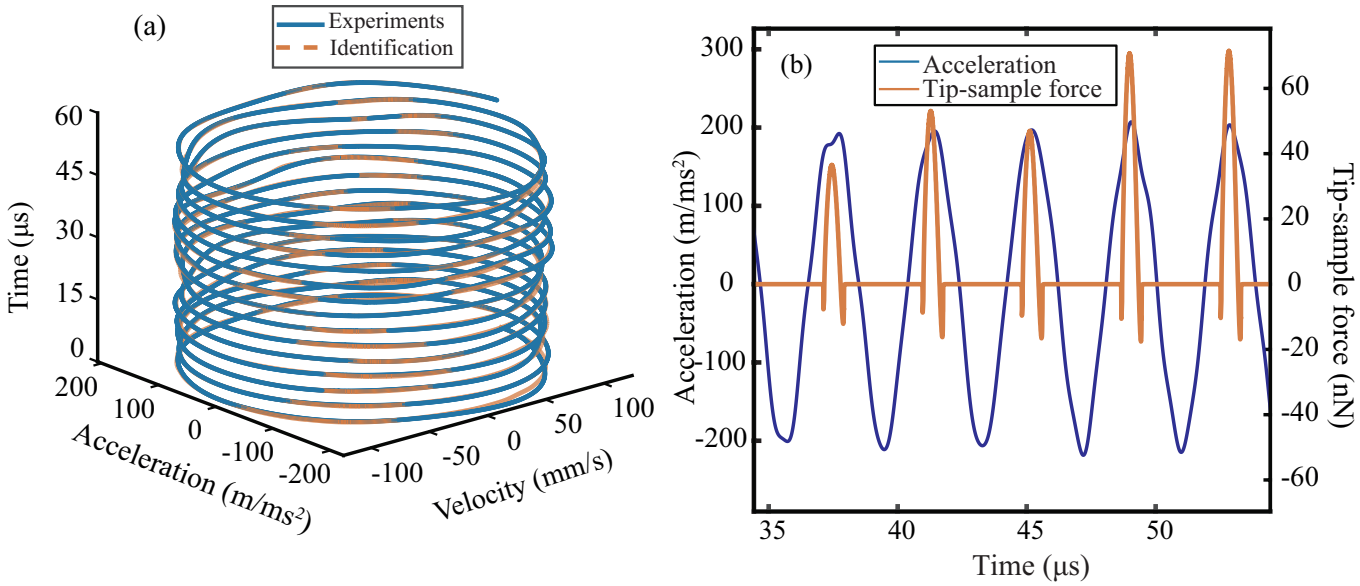

FIG. S2.9: Data-driven identification on silicon cantilever interacting with LDPE sample. The experimental deflection is obtained at a fixed tip-sample distance of 63.1 nm. (a) Identification of velocity and acceleration state vectors from data-driven model. The blue and orange curves represent the experimental and identified state space trajectories, respectively. (b) Estimation of the tip-sample force from data-driven model (orange) superimposed on the experimental acceleration signal (blue).

[1] S. I. Lee, S. W. Howell, A. Raman, and R. Reifenberger, Nonlinear dynamic perspectives on dynamic force microscopy, Ultramicroscopy **97**, 185 (2003).

[2] A. Chandrashekar, P. Belardinelli, S. Lenci, U. Staufer, and F. Alijani, Mode coupling in dynamic atomic force microscopy, Phys. Rev. Applied **15**, 024013 (2021).

[3] S. Rützel, S. I. Lee, and A. Raman, Nonlinear dynamics of atomic–force–microscope probes driven in lennard–jones potentials, Proceedings of the Royal Society of London. Series A: Mathematical, Physical and Engineering Sciences **459**, 1925 (2003).

[4] A. Chandrashekar, P. Belardinelli, U. Staufer, and F. Alijani, Robustness of attractors in tapping mode atomic force microscopy, Nonlinear Dynamics **97**, 1137 (2019).

[5] R. Garcia, C. J. Gómez, N. F. Martinez, S. Patil, C. Dietz, and R. Magerle, Identification of nanoscale dissipation processes by dynamic atomic force microscopy, Physical Review Letters **97**, 016103 (2006).

[6] E. T. Herruzo, A. P. Perrino, and R. Garcia, Fast nanomechanical spectroscopy of soft matter, Nat Commun **5**, 3126 (2014).

[7] S. Benaglia, V. G. Gisbert, A. P. Perrino, C. A. Amo, and R. Garcia, Fast and high-resolution mapping of elastic properties of biomolecules and polymers with bimodal afm, Nature Protocols **13**, 2890 (2018).

[8] D. Platz, D. Forchheimer, E. A. Tholen, and D. B. Haviland, Interaction imaging with amplitude-dependence force spectroscopy, Nature Communications **4**, 1360 (2013).

[9] R. Garcia and R. Perez, Dynamic atomic force microscopy methods, Surface Science Reports **47**, 197 (2002).

[10] H. V. Guzman, A. P. Perrino, and R. Garcia, Peak forces in high-resolution imaging of soft matter in liquid, ACS Nano **7**, 3198 (2013).